

# The role of absorption in three-dimensional electron diffraction dynamical structure refinement

Benjamin Colmey<sup>1</sup>, Tiarnan A.S. Doherty<sup>1,2</sup>, Shreshth A. Malik<sup>2</sup>, and Paul A. Midgley<sup>1</sup>

<sup>1</sup>Department of Materials Science and Metallurgy, University of Cambridge, 27 Charles Babbage Rd, Cambridge, CB3 0FS, United Kingdom

<sup>2</sup>OATML, Department of Computer Science, University of Oxford, Wolfson Building, Parks Rd, Oxford, OX1 3QG, United Kingdom

## Abstract

The role of absorption in 3D electron diffraction is established through analytical theory, simulation, and dynamical refinement. A two-beam expression for the absorbed integrated intensity is derived, showing that for  $t/\xi_g \ll 1$  reflections follow a uniform exponential decay set by the mean absorptive potential  $U'_0$ . Many-beam simulations demonstrate that neglecting absorption in dynamical refinement of integrated intensities incurs a residual that increases linearly with thickness and diverges near zone axes. Dynamical refinements were performed on  $\text{CsPbBr}_3$ , quartz, and borane, with the inclusion of absorption yielding an improvement in  $R_{\text{obs}}$  from 6.4 to 5.3 % for  $\text{CsPbBr}_3$  and negligible changes for quartz and borane. Absorption is therefore deemed negligible for routine refinement of integrated intensities except in high- $Z$  materials at thicknesses approaching  $\xi_g$ .

## 1 Introduction

Electron diffraction (ED) has become an established tool for determining the structures of nanocrystalline materials that are inaccessible to conventional X-ray crystallography. Developments such as precession electron diffraction (PED) [1] and continuous-rotation 3D ED have expanded its applicability, enabling routine structure determination across inorganic, hybrid, and molecular crystals [2].

Building on this foundation, dynamical refinement, as implemented in e.g. *JANA2020* [3], has enabled a continuing series of breakthroughs, including hydrogen localization [4], multipolar refinements [5] and ionisation-state analysis via  $\kappa$ -refinement [6]. Alternative formulations of dynamical refinement continue to be developed [7], extending the range and precision of these methods.

Refinement is the process by which a structural model is iteratively adjusted until convergence is achieved between simulated and observed diffraction intensities. Its accuracy is governed by the extent to which the scattering simulation reproduces the true physical interaction. The kinematical approach offers a simplified model, while dynamical simulation captures the full complexity of multiple scattering and can achieve far higher physical fidelity.

Despite these advances, inelastic scattering has generally been neglected in 3D ED refinement [8–10]. Such processes are known to alter diffracted intensities in ways not captured by purely elastic models [11]. Their omission thus limits the completeness of current refinements, potentially introducing artifacts into solved structures.

In high-energy ED, where accelerating voltages typically exceed 50 keV, incident electrons can exchange energy with the material through three inelastic mechanisms: thermal-diffuse scattering (TDS), plasmon excitations, and core-loss ionisation. Historically, the term *absorption* has been used to describe the effects arising from TDS. In reality, no true absorption occurs; rather, these processes lead to a loss of elastic intensity and a redistribution of diffracted intensity among beams [12], in contrast to the genuine absorption of photons in X-ray diffraction [13]. Here, it is worth noting that although many kinematical 3D ED refinements make use of X-ray software and absorption corrections [14–16], these corrections model a fundamentally different phenomenon.

While the electron-specific absorption formalism has previously been incorporated in convergent-beam electron diffraction (CBED) refinements [17–21] its use in 3D ED remains limited. Beyond CBED, absorption has been addressed through simulations of precession data using a constant absorptive potential, where comparisons with elastic-only calculations revealed only minor differences, but no systematic investigation of the impact of absorption on refinement was undertaken [9].

In CBED, a stationary crystal is illuminated by a convergent probe, producing Bragg discs that encode the full two-dimensional region surrounding a reciprocal-lattice vector. In 3D ED and PED, crystal rotation or beam precession integrates intensities over linear or circular trajectories, effectively averaging orientation-specific dynamical contrast. The consequence

is a set of integrated intensities that more closely match the kinematical approximation [22], making them well suited for structure solution techniques originally devised for X-ray data.

These considerations raise the central question: under what conditions does absorption materially influence structure refinement, and when can it safely be neglected? To address this, Bloch-wave simulations were performed with and without absorption across multiple materials and orientations, revealing its role on integrated intensities. Dynamical refinements including absorption were subsequently performed on experimental data, establishing the practical limits of the elastic-only approximation.

## 2 Methods

### 2.1 Thermal Effects in Quantitative Electron Diffraction

The present analysis builds upon the dynamical refinement method reported by Malik *et al.* [7], which implements a differentiable Bloch-wave framework. Unlike the kinematical approximation, which assumes single scattering, Bloch-wave methods explicitly account for coupling between diffracted beams.

Thermal vibrations in crystals give rise to diffuse scattering that removes electrons from the coherent diffracted beams, thereby producing an attenuation of diffracted intensities [23]. These effects can be decomposed into TDS, arising from random atomic displacements and phonon scattering [24, 25]. Both processes produce sub-eV energy losses that fall within the ‘zero-loss’ peak, rendering most commercially available energy filters ineffective at removing absorption effects and requiring treatment through cooling or explicit modeling [21].

While the original Bloch wave formalism developed by Bethe [26] treats only elastic scattering, absorption can be included through the complex Fourier coefficient of the potential [27]. For a reciprocal lattice vector  $\mathbf{g}$ , this coefficient can be written as [28]

$$U_{\mathbf{g}}^{\text{tot}} = U_{\mathbf{g}} + iU_{\mathbf{g}'} = -\frac{h^2}{2m_0\Omega} \sum_{\kappa} e^{-2i\pi(\mathbf{g}\cdot\mathbf{r}_{\kappa})} [f_{\kappa}(s) + if'_{\kappa}(s, B_{\kappa})] e^{-B_{\kappa}s^2} \quad (1)$$

where  $s = |\mathbf{g}|/2$ ,  $\mathbf{r}_{\kappa}$  is the position of atom  $\kappa$  in the unit cell,  $m_0$ ,  $h$ , and  $\Omega$  denote the electron rest mass, Planck’s constant, and the unit-cell volume, respectively. Here  $f_{\kappa}(s)$  is the elastic scattering factor and  $f'_{\kappa}(s, B_{\kappa})$  its absorptive counterpart, expressed in terms of  $s$  and the isotropic Debye–Waller factor  $B_{\kappa} = 8\pi^2\langle u_{\kappa}^2 \rangle$ , where  $\langle u_{\kappa}^2 \rangle$  is the mean-squared vibrational displacement. This displacement depends on the stiffness of the interatomic potential. Materials with high Debye temperatures ( $\Theta_D$ ) maintain relatively small  $\langle u^2 \rangle$

when compared to materials with low  $\Theta_D$  under the same conditions. Cooling reduces  $\langle u^2 \rangle$  and correspondingly diminishes the magnitude of the absorptive effects [12].

Despite its quantitative improvements over the elastic-only model, this formulation remains approximate. A principal limitation is the assumption that absorbed electrons are removed rather than redistributed into diffuse background intensity [12]. Although background subtraction mitigates the effect, it cannot fully separate diffuse inelastic contributions from the elastic signal.

Another important approximation concerns the use of isotropic atomic vibrations, represented by a single parameter  $U_{\text{iso}}$ , or calculated as  $U_{\text{iso}} = \frac{1}{3}(U_{11} + U_{22} + U_{33})$  when anisotropic displacement parameters are available. While anisotropic forms of  $f'_\kappa$  exist, they are considerably more demanding computationally, and the errors introduced in  $f'_\kappa$  by using isotropic Debye–Waller factors are typically on the order of 1–5 % for low- and medium-order reflections [29].

A further limitation arises from the use of the Einstein model, which assumes independent oscillators and fails to describe systems with strong phonon correlations. A more complete description is provided by the frozen phonon method [30, 31], which conserves total scattering intensity and recovers the diffuse background by averaging over many thermal configurations. While frozen phonon can be incorporated into the Bloch-wave framework [32, 33], it typically requires averaging over dozens of thermal configurations, imposing a computational burden that restricts its practical use in refinement.

## 2.2 Two-Beam Absorption Formalism

The two-beam approximation represents the simplest extension beyond the kinematical model, coupling the incident and a single diffracted beam while neglecting higher-order interactions. Although it fails to describe the complex coupling present in strongly diffracting systems or near high-symmetry zone axes, it is often valuable for analytical derivations and in theoretical interpretation.

The two-beam approximation gives analytical expressions for the diffracted-beam intensity under absorption [23]:

$$|\Psi_{\mathbf{g}}|_{\text{abs}}^2 = e^{(-2\kappa_0 t)} \frac{(\cosh(2\Delta\kappa t) - \cos(2\pi\Delta kt))}{2(1 + x^2)} \quad (2)$$

with the following definitions:

$$\begin{aligned}\kappa_0 &= \frac{\pi}{\xi'_0} & \Delta k &= \frac{\sqrt{1+x^2}}{\xi_g} & \Delta\kappa &= \frac{\pi}{\xi'_g\sqrt{1+x^2}} \\ \xi'_0 &= \frac{K}{U'_0} & \xi'_g &= \frac{K}{U'_g} & \xi_g &= \frac{K}{|U_g|} & x &= \xi_g S_g\end{aligned}$$

Here,  $S_g$  is the distance of a reciprocal lattice vector from the Ewald sphere surface and  $K$  is the radius of the Ewald sphere, given by  $K = 1/\lambda$ . The quantity  $\xi'_0$  determines the mean absorption, while  $\xi'_g$  governs the strength of anomalous absorption and may be regarded as an absorption distance, by analogy with the extinction distance  $\xi_g$ .

The mean absorptive potential  $U'_0$ , is defined as [34]

$$U'_0 = \frac{\gamma}{\pi} \frac{\sum_i n_i f'_i(0)}{\Omega}, \quad (3)$$

where  $\gamma$  is the relativistic correction factor,  $n_i$  are the site occupancies,  $f'_i(0)$  are the absorptive scattering factors at  $\mathbf{g} = 0$  and the sum is over all atoms in the unit cell. In the absence of absorption, the two-beam diffracted intensity simplifies to [35]:

$$|\Psi_{\mathbf{g}}|_{\text{no abs}}^2 = \frac{\sin^2(\pi t \Delta k)}{(1+x^2)}, \quad (4)$$

which can be rewritten as

$$|\Psi_{\mathbf{g}}|_{\text{no abs}}^2 = \frac{1 - \cos(2\pi t \Delta k)}{2(1+x^2)}, \quad (5)$$

In Eq. 2, absorption enters through a global damping term  $e^{-2\kappa_0 t}$  and a reflection specific term  $\cosh(2\Delta\kappa t)$ . When  $U'_0 = U'_g = 0$ , both reduce to unity, and Eq. 2 reverts to the elastic form of Eq. 5. While Eqs. 2 and 5 are given for diffraction at a specific orientation  $S_g$ , in 3D ED the quantity of interest is the integrated rocking-curve intensity. Starting from the non-absorbed two-beam expression (Eq. 5), the relevant quantity is

$$I_{\text{no abs}}^{\text{int}}(t) = \int_{-\infty}^{\infty} |\Psi_{\mathbf{g}}|_{\text{no abs}}^2 dx, \quad x = \xi_g S_g \quad (6)$$

This integral has the well-known analytical form first derived by Blackman [22]. Introducing  $A = \pi t / \xi_g$ , one obtains

$$I_{\text{no abs}}^{\text{int}}(t) \approx \int_{-\infty}^{\infty} \frac{\sin^2(A\sqrt{1+x^2})}{1+x^2} dx \approx 2 \int_0^A J_0(2u) du, \quad (7)$$

where  $J_0$  is the Bessel function of the first kind. As derived in Supplementary Section S1, carrying out the same integral for the absorbed case in the weak-absorption limit ( $t/\xi_g \ll 1$ ) yields

$$I_{\text{abs}}^{\text{int}}(t) \approx e^{-2\kappa_0 t} I_{\text{no abs}}^{\text{int}}(t) \left[ 1 + \frac{\pi^2 t \xi_g}{2\xi_g'^2} \left( 1 - \frac{\pi^2 t^2}{12\xi_g^2} \right)^{-1} \right], \quad (8)$$

Absorption therefore modifies the integrated two-beam intensity in two distinct ways. The global factor  $e^{-2\kappa_0 t}$  applies a uniform thickness-dependent attenuation, given by  $U'_0$ . The second factor represents the anomalous contribution arising from the reflection-specific  $U'_g$ . At large thickness, this anomalous term causes reflections to diverge from the uniform decay. Reflections with large  $U'_g$  (small  $\xi'_g$ ) show the largest departures, since the anomalous term scales approximately as  $\xi_g/\xi_g'^2$ .

To obtain experimentally meaningful quantities, the two-beam integrated expressions must include an additional Lorentz correction. This correction accounts for the angular dwell time of a reflection near its Bragg condition, which is inversely proportional to the velocity of Bragg-crossing during rotation [36, 37].

In a continuous rotation experiment, this velocity is set by the component of the reciprocal-lattice vector perpendicular to the rotation axis [38]. If  $\phi$  denotes the angle between  $\mathbf{g}$  and the rotation axis, the intersection speed is proportional to  $|\mathbf{g}| \sin \phi$ . The correction therefore takes the form  $L = 1/|\mathbf{g}| \sin \phi$ , which expresses the fact that reflections near the rotation axis remain near their Bragg condition for longer and contribute more strongly to the observed experimental intensity.

## 3 Results

### 3.1 Comparison of Two- and Many-Beam Models of Absorption

The material caesium lead bromide ( $\text{CsPbBr}_3$ ) was examined using the structure reported in [6], with the corresponding structural parameters listed in Table 1. This compound was selected because it contains atoms of large atomic number and correspondingly strong elastic and absorptive scattering factors  $f$  and  $f'$ , making absorption especially significant.

Two-beam and many-beam integrated intensities were simulated for  $\text{CsPbBr}_3$  at 200 keV using the first experimentally observed orientation,  $[uvw] = [-1.0, 0.39, -0.53]$ . This orientation defines the centre of a virtual frame, as described in [39], with each virtual frame corresponding to a small angular range in  $\alpha$  around the central orientation, where  $\alpha$  is the rotation axis of the goniometer. In this study, all orientations correspond to experimentally observed ones, while specific angular positions within a virtual frame are referred to as tilts.

The two-beam integrated intensities for this orientation were computed by numerically integrating Eqs. (2) and (4) with an additional Lorentz correction. In the many-beam case, calculations were performed using the full Bloch-wave code described in [7], with the parametrized form of the absorptive scattering factors  $f'$  adapted from [10]. Here, no Lorentz correction is required because the rotation geometry is already encoded through explicit tilt sampling.

A  $\pm 1.5^\circ$  sweep around the experimental orientation was simulated with 60 uniformly spaced tilt samples, and the corresponding rocking curves were summed to obtain the integrated intensities. Unless otherwise stated, 60 tilt samples per orientation were used throughout.

Simulations were performed for thicknesses between 10-250 nm. This lower limit was chosen as the width of rocking curves scale inversely with thickness in the kinematic limit [35], and therefore at very small thicknesses (where the kinematic approximation is valid), the curves may exceed the angular range defined by the virtual frame. As a result, part of the diffracted intensity may fall outside the sampling window, making these reflections not fully-integrated.

The resulting two-beam and many-beam integrated intensities, with and without absorption, are shown in Fig. 1.

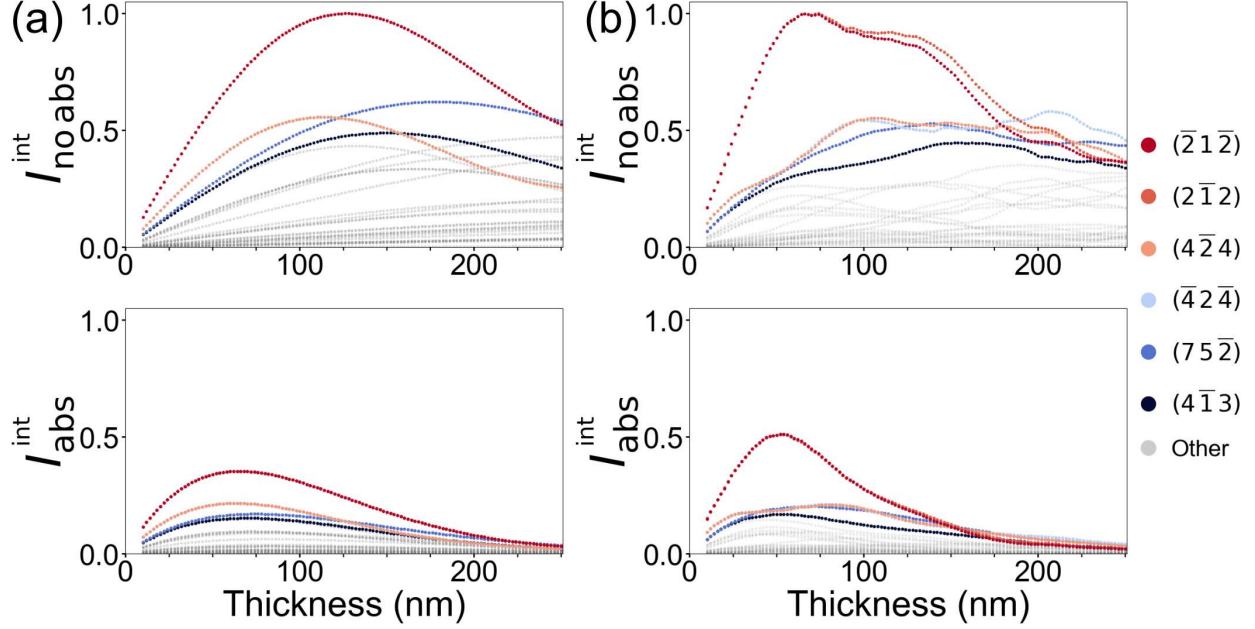


Figure 1: Integrated intensity vs thickness for  $CsPbBr_3$ , 200 keV,  $[uvw] = [-0.43, 1.00, 0.93]$ , without (top) and with absorption (bottom), for (a) two-beam, (b) many-beam model. The six most intense reflections are highlighted in colour, with all others shown in grey for clarity.

While the two-beam curves show smooth Pendellösung-type oscillations, the many-beam case develops the expected irregularities from multiple strongly coupled reflections. In the two-beam model, pairs such as  $(\bar{2} \bar{1} \bar{2})/(2 \bar{1} 2)$  and  $(4 \bar{2} 4)/(\bar{4} 2 \bar{4})$  maintain identical intensities over the full thickness range. In the many-beam calculation, however, these pairs begin to diverge at thicknesses approaching 100 nm, reflecting the redistribution of intensity through additional dynamical pathways.

In both models, absorption clearly attenuates intensities, but this plot alone does not reveal the reflection-specific decay rates or how the models compare. To address this comparison, Fig. 2 shows the ratio of absorbed to non-absorbed integrated intensities ( $I_{\text{abs}}^{\text{int}}/I_{\text{no abs}}^{\text{int}}$ ) as a function of thickness for the two and many-beam models.

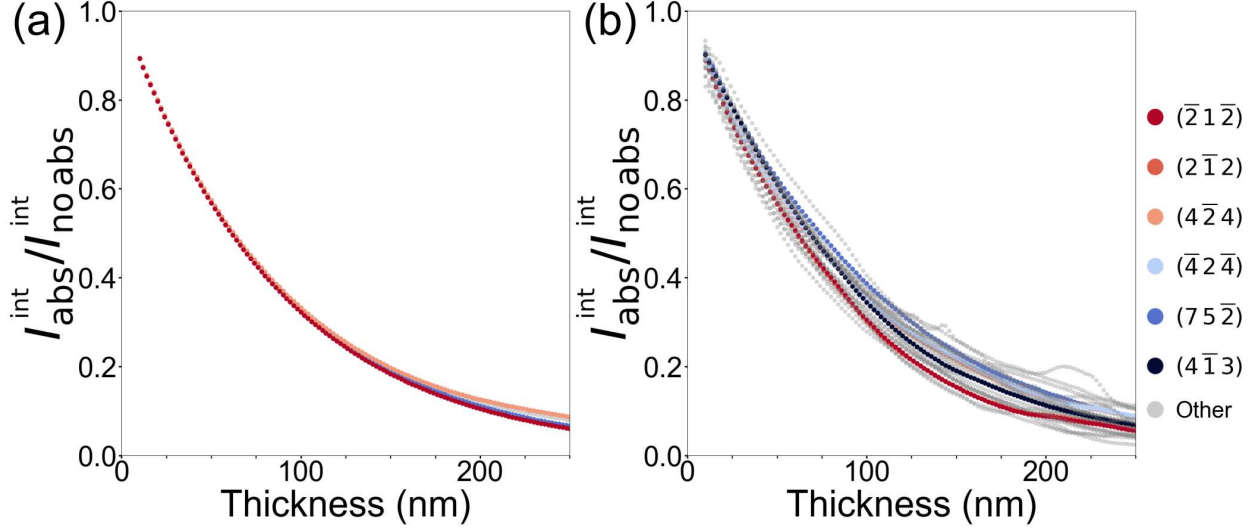


Figure 2: Ratio of integrated intensity ( $I_{\text{abs}}^{\text{int}}/I_{\text{noabs}}^{\text{int}}$ ) as a function of thickness for  $\text{CsPbBr}_3$  with  $[uvw] = [-0.43, 1.00, 0.93]$ . (a) Two-beam model; (b) many-beam model. A decaying exponential was fitted to each  $hkl$  curve, yielding absorption parameters  $\bar{\lambda} = 89.9 \text{ nm}$ ,  $\sigma_\lambda = 2.0 \text{ nm}$  (two-beam) and  $\bar{\lambda} = 93.2 \text{ nm}$ ,  $\sigma_\lambda = 10.1 \text{ nm}$  (many-beam).

In the two-beam case (Fig. 2(a)), fitting an exponential decay to each individual  $hkl$  yields a mean absorption length of  $\bar{\lambda} = 89.9 \text{ nm}$  with a standard deviation of  $\sigma_\lambda = 2.0 \text{ nm}$ . From the two-beam absorption formalism, the decay constant is determined by the global damping term, with  $\lambda_{\text{2-beam}} = K/(2\pi U'_0)$ . Using  $K = 39.87 \text{ \AA}^{-1}$  at 200 keV and  $U'_0 = 0.0072 \text{ \AA}^{-2}$  for  $\text{CsPbBr}_3$ , the predicted absorption length is  $\lambda_{\text{2-beam}} = 88.4 \text{ nm}$ , in excellent agreement with the fitted value.

As expected, the two-beam model shows little reflection-dependent variation in the absorption ratios.  $(4\bar{2}4)$  and  $(\bar{4}2\bar{4})$  begin to deviate for  $t > 150 \text{ nm}$  ( $(4\bar{2}4)$  is not visible because it lies directly beneath  $(\bar{4}2\bar{4})$ ). These reflections have the largest values of  $U_g$  and  $U'_g$  among the observed set, with  $U_g = 0.013 \text{ \AA}^{-2}$ ,  $U'_g = 0.003 \text{ \AA}^{-2}$ , giving  $\xi_g \approx 300 \text{ nm}$  and  $\xi'_g \approx 1400 \text{ nm}$ . Eq. 8 predicts that the anomalous contribution increases when  $t$  approaches  $\xi_g$ , in agreement with the observed behaviour.

By contrast, the many-beam case (Fig. 2(b)) exhibits a broader distribution of decay constants, with  $\bar{\lambda} = 93.2 \text{ nm}$  with  $\sigma_\lambda = 10.1 \text{ nm}$ , indicative of the effects of anomalous, reflection-specific absorption.

Beyond integrated intensities, rocking-curve analysis provides further insight into how absorption modifies scattering pathways. Many-beam rocking curves for all reflections considered in the above calculation at  $t = 200 \text{ nm}$  are shown in Supplementary Fig. S2. While

not representative of the original sample thickness observed in [6], 200 nm serves as an illustrative high-thickness example, where absorption is especially pronounced.

Supplementary Fig. S2 shows that absorption can modify the tilt-dependent intensity profile (i.e. rocking curve) in ways that vary markedly across reflections: for some, the effect is nearly uniform across all tilts, while for others it is strongly tilt dependent. Despite these local tilt variations, the corresponding integrated intensities exhibit far smaller differences between absorptive and elastic simulations. This contrast helps explain why absorption plays a significant role in CBED analysis, where rocking-curve shapes are fitted directly [18], but a reduced one in 3D ED, where integration suppresses tilt-specific behaviour.

### 3.2 Implications of Neglecting Absorption in Dynamical Refinement

The discrepancy between elastic and absorptive simulations can be further quantified using a residual. A standard choice is  $R_1$ , defined as

$$R_1 = \frac{\sum_i \left| \sqrt{I_i^{\text{exp}}} - \sqrt{I_i^{\text{calc}}} \right|}{\sum_i \sqrt{I_i^{\text{exp}}}}.$$

where  $I_i^{\text{exp}}$  denotes the experimentally observed intensity of reflection  $i$ , and  $I_i^{\text{calc}}$  the corresponding simulated intensity. Because  $R_1$  does not weight reflections by their experimental uncertainties, it is particularly sensitive to noisy, low-intensity reflections. Consequently, practical refinements typically report  $R_{\text{obs}}$ , defined as  $R_1$  evaluated only over reflections satisfying  $I_i^{\text{exp}}/\sigma_i > 3$ , where  $\sigma_i$  is the estimated measurement error [40]. Another alternative is the weighted form  $wR_{\text{all}}$ , which considers all intensities and weights the contribution of each  $I_i$  according to its uncertainty  $\sigma_i$  and its magnitude. To estimate the influence of absorption,  $R_1$  can be adapted to measure the deviation between absorptive and purely elastic simulations.

$$R_1(t) = \frac{\sum_i \left| \sqrt{I_i^{\text{int,abs}}(t)} - \sqrt{I_i^{\text{int,no abs}}} \right|}{\sum_i \sqrt{I_i^{\text{int,no abs}}}}, \quad (9)$$

If the ratio of integrated intensities  $I_i^{\text{int,abs}}/I_i^{\text{int,no abs}}$  is approximated as an exponential decay with mean decay constant  $\bar{\lambda}$  and a Gaussian spread of  $\lambda_i$ , the resulting thickness-dependence of the residual can be estimated in closed form. As derived in the Supplementary Section

S2, the expected residual as a function of thickness is given by:

$$R_1(t) \approx \sqrt{\frac{2}{\pi}} \frac{t \sigma_\lambda}{2 \bar{\lambda}^2}, \quad R_1(t) \propto t \quad (10)$$

so that the slope of the residual is

$$\frac{dR_1}{dt} = \sqrt{\frac{2}{\pi}} \frac{\sigma_\lambda}{2 \bar{\lambda}^2}. \quad (11)$$

$R_1$  is therefore expected to increase linearly with thickness, governed by both the mean absorption length  $\bar{\lambda}$  and its relative spread  $\sigma_\lambda$ . A uniform absorptive attenuation, such as that predicted by the two-beam model, is therefore expected to have no impact on residuals, in contrast to the anomalous absorption observed in many-beam simulations.

To test this, Eq. 9 was evaluated across thickness for  $\text{CsPbBr}_3$  at  $[uvw] = [-0.43, 1.00, 0.93]$ , with the results shown in Fig. 3(a). Although the comparison involves only simulated intensities, the calculation was restricted to reflections classified as experimentally observed in the original dataset, with  $I_i^{\text{exp}}/\sigma_i > 3$ , to ensure a consistent and fair comparison with experiment.

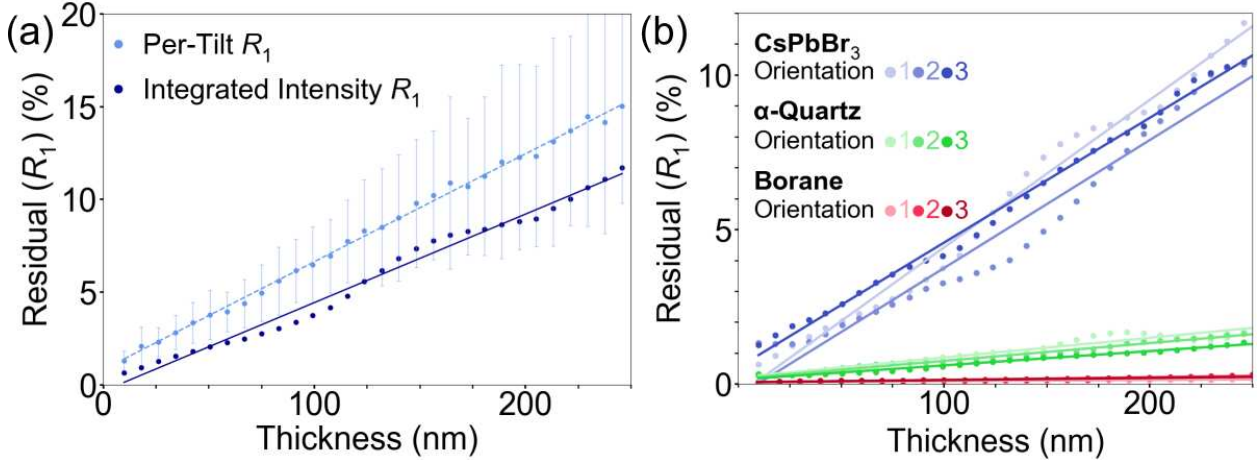


Figure 3: Thickness dependence of residual error  $R_1$  (%), between simulated  $I_{\text{abs}}$  and  $I_{\text{no abs}}$ . (a) Integrated intensities (dark blue) compared with per-tilt intensities (light blue) for  $\text{CsPbBr}_3$  at  $[uvw] = [-0.43, 1.00, 0.93]$ ; light blue points are  $R_1$  averages across  $\pm 1.5^\circ$  tilt-series with error bars showing standard deviation around the mean. Best-fit slopes were determined, yielding  $0.048 \text{ \% nm}^{-1}$  and  $0.058 \text{ \% nm}^{-1}$  for the integrated intensities and per-tilt values, respectively. (b) Integrated-intensity  $R_1$  curves for  $\text{CsPbBr}_3$ ,  $\alpha$ -quartz, and borane, each shown with three representative orientations (best-fit slopes and  $[uvw]$  indices given in Supplementary Table 1.)

In Fig. 3(a), the dark blue curve is calculated from integrated intensities, obtained by summing 60 tilts across the full  $\pm 1.5^\circ$  tilt series, while residuals at individual tilts (non-integrated intensities) are shown in light blue. The comparison demonstrates reduced anomalous absorption achieved by integration: although individual tilts can show strong deviations, these largely cancel when averaged.

At low thicknesses the predicted effect of absorption is minimal, with  $R_1$  remaining below 5% for thicknesses under 100 nm. Using the parameters  $\bar{\lambda} = 93.2$  nm and  $\sigma_\lambda = 10.1$  nm, the predicted slope from Eq. (11) is  $\frac{dR_1}{dt} = 0.046\% \text{ nm}^{-1}$ , in close agreement with the best-fit slope of  $0.048\% \text{ nm}^{-1}$  shown in Fig. 3(a).

This residual can be interpreted as a nominal attainable lower bound on an elastic-only dynamical refinement. To compare this predicted lower bound with real refinements, we consider the elastic-only refinements of the same  $\text{CsPbBr}_3$  dataset reported by Suresh *et al.* and re-analysed by Malik *et al.* [7]. Suresh *et al.* reported an overall  $R_{\text{obs}} = 5.3\%$ , while Malik *et al.* yielded a value of  $R_{\text{obs}} = 6.5\%$ . Because the present study employs the refinement framework and simulation pipeline of Malik *et al.*, all comparisons refer specifically to their results, ensuring that parameters are defined and controlled consistently.

While the true specimen thickness is not known, the hybrid physics-machine learning framework used in this study and introduced in [7] extracts an orientation-dependent thickness distribution directly from the diffraction data through joint refinement of structural and experimental parameters. For the orientation shown in Fig. 3(a), this corresponds to a thickness of  $t \approx 50$  nm, for which the predicted effect of neglecting absorption is around 2%. This comparison shows that the low refinement residuals reported are consistent with the predicted effect of absorption at this thickness, indicating that only a minor improvement would be expected from incorporating absorption in the refinement.

While the preceding comparison concerns only a single orientation, absorption and resulting residuals are expected to vary with orientation. To quantify this effect,  $R_1(t)$  between absorptive and purely elastic simulations was computed for a range of orientations and materials typical of 3D ED experiments. Figure 3(b) compares these results for three materials taken from recently reported continuous-rotation 3D ED datasets:  $\text{CsPbBr}_3$  [6],  $\alpha$ -quartz [39], and octadecaborane (hereafter referred to as borane) [6]. In each case, the first three experimentally observed orientations were simulated, with Eq. 9 evaluated only for reflections with  $I_i^{\text{exp}}/\sigma_i > 3$ . These materials were selected to capture a wide range of structural and physical characteristics:  $\text{CsPbBr}_3$  is a halide perovskite with high atomic number, quartz is an inorganic oxide with moderate atomic number, and borane is an inor-

ganic molecular crystal composed of light elements. Their crystallographic parameters are listed in Table 1.

Table 1: Crystallographic parameters for the three materials used in this study.

Parameters	<b>CsPbBr<sub>3</sub></b>	<b><math>\alpha</math>-quartz (SiO<sub>2</sub>)</b>	<b>Borane (B<sub>18</sub>H<sub>22</sub>)</b>
Source dataset	[6]	[39]	[6]
Space group	<i>Pbnm</i>	<i>P3<sub>2</sub>1</i>	<i>Pcnn</i>
Unit cell ( <i>a</i> , <i>b</i> , <i>c</i> ) (Å)	8.119, 8.359, 11.759	4.923, 4.923, 5.400	10.770, 11.990, 10.736
Angles ( $\alpha$ , $\beta$ , $\gamma$ ) (°)	90, 90, 90	90, 90, 120	90, 90, 90
Volume (Å <sup>3</sup> )	798.1	113.3	1386.9

From Fig. 3(b), clear material-dependent trends emerge. For all three materials, the first three orientations lie within a narrow mean-thickness range, giving values of approximately 50 nm for CsPbBr<sub>3</sub>, 85 nm for  $\alpha$ -quartz, and 170 nm for borane, as determined from the orientation-dependent thickness profile obtained in the elastic-only refinements (See Supplementary Fig. S5). At these thicknesses, absorption contributes ca. 2% for CsPbBr<sub>3</sub>, 0.6% for  $\alpha$ -quartz, and 0.2% for borane.

As shown earlier, in the two-beam limit, inclusion of absorption produces almost no per-reflection variation, with intensities attenuated uniformly. Under many-beam conditions, however, absorption alters the inter-beam coupling, changing how intensity is redistributed with thickness. The resulting deviation from the elastic-only solution therefore reflects the degree of many-beam interaction. In CsPbBr<sub>3</sub>, the heavy constituent atoms lead to the simultaneous excitation of many strong beams. In contrast,  $\alpha$ -quartz and borane exhibit much weaker many-beam character at these thicknesses. Their lower atomic numbers result in fewer simultaneously excited strong reflections, so scattering is dominated by quasi-two-beam interactions. In such regimes, the inclusion of absorption does not result in significant redistribution of diffracted intensity.

### 3.3 Orientation Dependence of Absorption Effects

In addition to the strong material dependence, little systematic variation is observed across orientations in Fig. 3(b). This may be explained by the geometry of the orientations examined, with each lying away from strongly diffracting zone axes. This behaviour is characteristic of 3D ED datasets, where randomly orientated crystals are rotated through large angular ranges that remain predominantly off-zone, typically intersecting perhaps only a single major zone axis over the course of the tilt series. At such zone-axis conditions, however,

where many-beam effects are strongest, a correspondingly greater influence of absorption is expected.

To examine this behaviour explicitly, three representative orientations from the  $\text{CsPbBr}_3$  dataset were selected to span off-zone, intermediate, and near-zone regimes. While several orientations in the dataset fall into each category, orientations 1, 8, and 19 were chosen for illustration, with the corresponding simulated diffraction patterns shown in Fig. 4(b). Orientation 1 ( $[uvw]=[-0.43, 1.00, 0.93]$ ) serves as the representative off-zone reference, orientation 8 ( $[uvw]=[-0.67, 1.00, 0.67]$ ) corresponds to a direction near  $[\bar{2}32]$ , and orientation 19 ( $[uvw]=[-1.00, 1.00, 0.33]$ ) lies close to  $[\bar{3}31]$ .

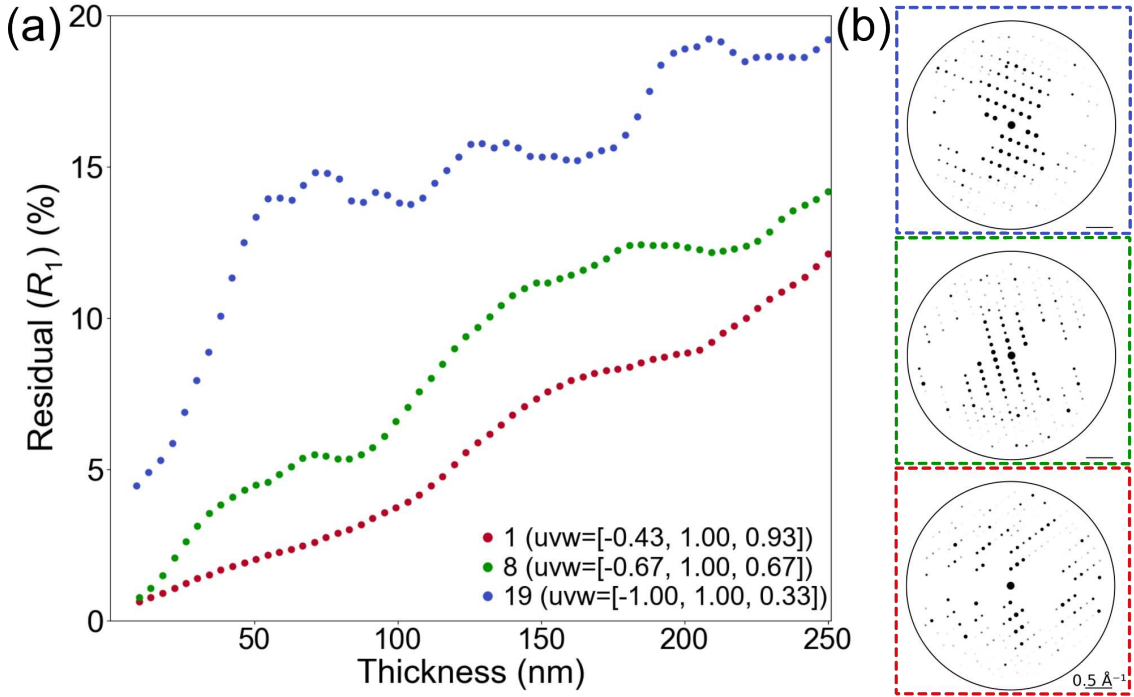


Figure 4: Orientation dependence of absorption effects in  $\text{CsPbBr}_3$ . (a) Thickness dependence of  $R_1$  between simulated  $I_{\text{abs}}^{\text{int}}$  and  $I_{\text{no abs}}^{\text{int}}$  for orientations 1, 8, and 19. (b) Corresponding simulated diffraction patterns, each enclosed by a dashed box in the colour of its respective curve in (a).

In Fig. 4(a), the variation of  $R_1(t)$  with crystal orientation is shown, highlighting the strengthening of many-beam coupling and the associated enhancement of anomalous absorption effects as the crystal is tilted toward a strongly diffracting zone axis. Orientation 1 (seen previously in Fig. 3 (a,b)) is representative of most orientations in the dataset, with an approximately linear thickness dependence in  $R_1$ . Orientation 8 displays a markedly steeper

trend, indicating stronger many-beam coupling, while orientation 19 shows the strongest and most nonlinear response, rising to nearly 13% by 50 nm. Such a large residual indicates that an elastic-only refinement would perform poorly for this orientation, with a correspondingly large improvement expected if absorption is included.

Further insight into this behaviour is provided in Supplementary Fig. S3, in which  $I_{\text{abs}}^{\text{int}}/I_{\text{no abs}}^{\text{int}}$  is plotted as a function of thickness for the corresponding curves. These simulations show that the decaying-exponential attenuation underlying the linear  $R_1(t)$  trend no longer holds as the crystal approaches a zone axis.

Comparable behaviour has been reported in recent dynamical refinements, where orientations near zone axes exhibit anomalously high residuals, previously ascribed to crystal imperfections and excessive dynamical effects [5]. In that study, fifteen frames corresponding to these orientations were omitted from the refinement, representing a significant loss of usable data. The present results indicate that exclusion of such frames may be unwarranted, as the elevated residuals are largely attributable to previously unmodelled absorption effects.

### 3.4 Elastic and Absorptive Refinements of Experimental 3D-ED Data

Although the preceding simulations indicate that the inclusion of absorption will significantly alter simulated intensities, it remains unclear whether these differences will yield measurable benefits in refinement accuracy or in the recovered structure. To answer this question, full dynamical refinements were carried out for  $\text{CsPbBr}_3$ ,  $\alpha$ -quartz and borane, with and without absorption.

For each material, refinements followed the complete workflow described in [7]. This included orientation-dependent thicknesses refinements. The corresponding refined thickness–tilt curves for all three materials are shown in Supplementary Fig. S5; overall the absorptive and elastic models give similar trends, but notable deviations occur for specific orientations (e.g.,  $\text{CsPbBr}_3 \sim 55$  vs 48 nm; borane  $\sim 200$  vs 170 nm).

The corresponding refined thickness–tilt curves for all three materials are shown in Supplementary Fig. S5. The resulting refinement statistics are summarised in Table 2, with refinement parameters provided in Supplementary Table 2.

Table 2: Refinement residuals for  $\text{CsPbBr}_3$ ,  $\alpha$ -quartz, and borane.

Residual (%)	$\text{CsPbBr}_3$	$\alpha$ -quartz	Borane
Elastic $R_{\text{obs}}/wR_{\text{all}}$	6.40 / 6.73	4.14 / 3.84	9.54 / 8.56
Absorptive $R_{\text{obs}}/wR_{\text{all}}$	5.26 / 5.31	4.00 / 3.66	9.48 / 8.51

Across all three materials, the inclusion of absorption produces only modest changes in the refinement residuals.  $\text{CsPbBr}_3$  shows a clear improvement when absorption is included, while the refinements residuals of  $\alpha$ -quartz and borane remain effectively unchanged.

While the earlier analysis predicted a reduction of  $R_{\text{obs}}$  for  $\text{CsPbBr}_3$  from approximately 6.4% to 4.5%, the refinement only reaches 5.3 %. This outcome likely reflects both the simplifying assumptions of the absorptive model, including its isotropic treatment of thermal motion and unmodelled phonon correlations, and the broader set of factors that contribute to the observed residual, such as plasmon and core-loss ionisation, beam damage, and crystal imperfections. These factors obscure the specific contribution of absorption, and the observed decrease in  $R_{\text{obs}}$  is therefore consistent with the expected behaviour under experimental conditions.

For quartz and borane, the predicted absorption effects were modest, and the refinements exhibit correspondingly small improvements. For both materials, absorption therefore plays no significant role in the refinement, and the remaining analysis focuses on  $\text{CsPbBr}_3$ , with the full quartz and borane results reported in the Supplementary Material.

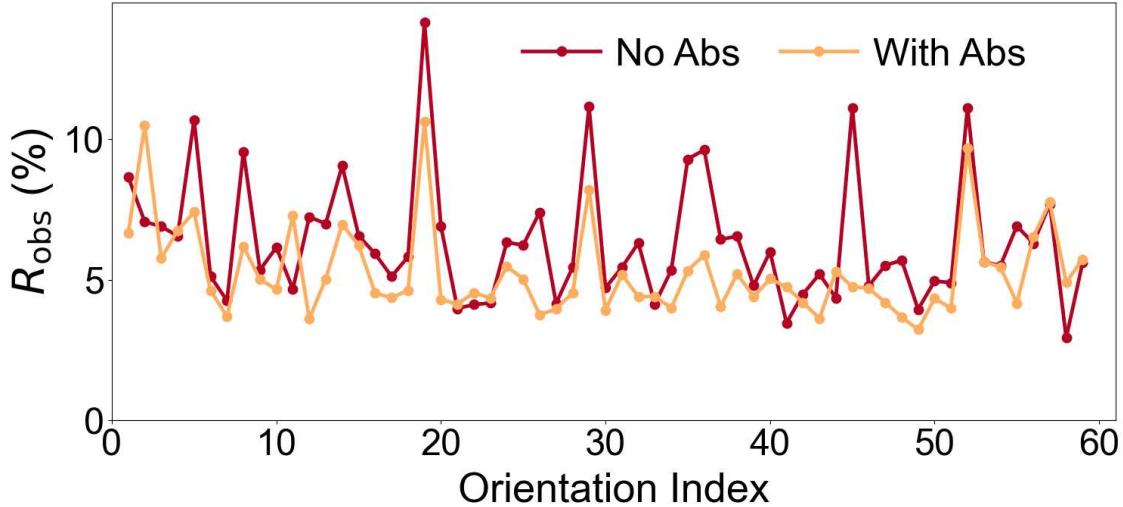


Figure 5: Results of dynamical refinements performed with and without the inclusion of absorption for  $\text{CsPbBr}_3$ . Residuals  $R_{\text{obs}}$  (%) are compared across rotation indices for refinements carried out on identical datasets and parameters. Supplementary Fig. S4 shows the corresponding  $wR_{\text{all}}$  results for  $\text{CsPbBr}_3$  and the full orientation-dependent residuals for  $\alpha$ -quartz and borane.

Beyond the overall improvement in residuals observed for  $\text{CsPbBr}_3$ , the orientation-dependent residuals (Fig. 5) show several pronounced outliers (orientations 19, 29, 46, 53). As discussed in Section 3.2, these orientations lie near strongly diffracting zone axes, where many-beam coupling is stronger and absorption has a larger influence.

Although the residuals of orientations 19, 29, 53 decrease markedly following the inclusion of absorption, they remain high outliers. This behaviour indicates that the present absorptive model corrects only part of the deviation and that additional zone-axis effects, possibly including plasmon and core-loss ionisation contributions or more complex dynamical interactions, remain unaccounted for. While such orientations might warrant exclusion in an elastic-only refinement, the absorptive model provides a sufficient basis for their retention.

Additionally, several orientations exhibit worse residuals under the absorptive model. While it is not clear why this occurs, it likely reflects the non-convex nature of the refinement, in which the search trajectory may settle into a suboptimal local minimum.

To further assess the consequences of including absorption on the refined structure, Supplementary Table S3 compares the atomic parameters obtained with and without the absorptive potential for  $\text{CsPbBr}_3$ . The inclusion of absorption produces only minor shifts in both fractional coordinates and anisotropic displacement parameters. The largest observed

positional difference is approximately 0.001 in fractional coordinates, with corresponding changes in anisotropic displacement parameters below  $0.003 \text{ \AA}^2$ , both within normal refinement precision [41], confirming that the refined structure remains stable under the modified scattering model. This indicates that even for a material with large mean atomic number  $\langle Z \rangle$  of 48.4, for thicknesses below 50 nm, absorption has little practical impact on the recovered structure. Consequently, omitting absorption from dynamical refinement simulation is expected to bias thermal and structural parameters only in high- $Z$  materials at thickness approaching  $\xi_g$ .

## 4 Conclusion

This work presents what is, to our knowledge, the first implementation of absorption in 3D ED dynamical refinement, establishing its influence on experimental residuals and refined structures. Though central to CBED contrast, absorption has a much weaker influence on the relative intensities measured in 3D ED. This discrepancy arises from integration, which averages orientation-specific anomalous absorption.

The underlying theory is examined, beginning from the two-beam approximation, yielding a closed form expression for integrated intensities in the presence of absorption. This shows that for  $t \ll \xi_g$  reflections experience a uniform exponential decay with thickness, with a decay rate set by the mean absorptive potential  $U'_0$ . In the many-beam limit, dynamical refinements that neglect absorption incur a systematic, thickness-dependent residual. The residual  $R_1(t)$  grows approximately linearly with thickness, determined by the mean absorption length  $\bar{\lambda}$  and its spread  $\sigma_\lambda$ , and diverging near zone axes. This behaviour explains a longstanding observation that orientations near zone axes exhibit anomalously high residuals in elastic-only dynamical refinements and provides a framework for incorporating these data rather than discarding them.

Comparative refinements of  $\text{CsPbBr}_3$  performed with and without absorption show a clear improvement in fit when absorption is included, reducing the refinement residual  $R_{\text{obs}}$  from 6.4 % to 5.3 %. In contrast, refinements of  $\alpha$ -quartz and borane under identical conditions show little improvement in  $R_{\text{obs}}$ , consistent with expectations for lower- $Z$  materials.

Absorption can therefore safely be neglected for routine refinements except in high- $Z$  materials for thicknesses approaching  $\xi_g$ . Although not addressed in the present analysis, temperature is also expected to play a significant role, with materials observed at  $T \geq \Theta_D$  likely to exhibit strong absorptive effects.

Additionally, the influence of omitting absorption in the determination of finer structural information such as bonding charge density remains unclear. It is worth noting that deviations away from neutral atom scattering factors will effect low-order reflections disproportionately. These have, in general, the largest  $U_g, U'_g$  and the effects of absorption will likely be appreciable.

## Acknowledgements

The authors thank Lukas Palatinus and his co-workers for access to their 3D ED data used in this work. The authors would further like to thank Lukas Palatinus, Ondrej Krivanek, Colin Humphreys, Mike Treacy, Petr Vacek, Hannah Cole and Simon Fairclough for helpful discussions.

## Funding

BC acknowledges funding from Queens' College Cambridge and the Stamps Scholars Program. TASD acknowledges the support of a Schmidt Science Fellowship. SM acknowledges funding from EPSRC Centre for Doctoral Training in Autonomous Intelligent Machines and Systems (Grant No: EP/S024050/1). PAM acknowledges funding from the Engineering and Physical Sciences Research Council (Nos. EP/W522120/1 and EP/R008779/1).

## Conflicts of Interest

The authors disclose no conflicts of interest.

## Data Availability

All data, analyses, and code used to produce the results are available in the GitHub repository [bcolmey/role-of-absorption-in-3DED-dynamical-refinement](https://github.com/bcolmey/role-of-absorption-in-3DED-dynamical-refinement).

## References

- [1] R. Vincent and P. A. Midgley. “Double conical beam-rocking system for measurement of integrated electron diffraction intensities”. In: *Ultramicroscopy* 53.3 (1994), pp. 271–282.
- [2] Mauro Gemmi et al. “3D Electron Diffraction: The Nanocrystallography Revolution”. In: *ACS Central Science* 5.8 (2019). Open Access, pp. 1315–1329. DOI: 10.1021/acscentsci.9b00394.
- [3] Václav Petříček et al. In: *Zeitschrift für Kristallographie - Crystalline Materials* 238.7-8 (2023), pp. 271–282. DOI: doi:10.1515/zkri-2023-0005.
- [4] Lukáš Palatinus et al. “Hydrogen positions in single nanocrystals revealed by electron diffraction”. In: *Science* 355 (2017), pp. 166–169. DOI: 10.1126/science.aal3003.
- [5] Barbara Olech et al. “Dynamical refinement with multipolar electron scattering factors”. In: *IUCrJ* 11 (2024), pp. 309–324. DOI: 10.1107/S2052252524001763.
- [6] Ashwin Suresh et al. “Ionisation of atoms determined by kappa refinement against 3D electron diffraction data”. In: *Nature Communications* 15 (2024), p. 9066. DOI: 10.1038/s41467-024-53448-2.
- [7] Shreshth A. Malik et al. “Hybrid Physics-Machine Learning Models for Quantitative Electron Diffraction Refinements”. In: *arXiv preprint arXiv:2508.05908* (2025). DOI: 10.48550/arXiv.2508.05908. arXiv: 2508.05908 [physics.comp-ph].
- [8] Ambarneil Saha et al. “Electron Diffraction of 3D Molecular Crystals”. In: *Chemical Reviews* 122.17 (2022). PMID: 35970513, pp. 13883–13914. DOI: 10.1021/acs.chemrev.1c00879. eprint: <https://doi.org/10.1021/acs.chemrev.1c00879>.
- [9] Lukáš Palatinus et al. “Structure refinement from precession electron diffraction data”. In: *Acta Crystallographica Section A: Foundations of Crystallography* 69 (2013), pp. 171–188. DOI: 10.1107/S0108767312048171.
- [10] M. Thomas et al. “Parameterized absorptive electron scattering factors”. In: *Acta Crystallographica Section A: Foundations and Advances* 80.2 (2024), pp. 146–150. DOI: 10.1107/S2053273323010963.
- [11] Alexander S. Eggeman et al. “Aberration-corrected and energy-filtered precession electron diffraction”. In: *Zeitschrift für Kristallographie* 228 (2013), pp. 43–50. DOI: 10.1524/zkri.2013.1565.

[12] C. J. Humphreys and P. B. Hirsch. “Absorption parameters in electron diffraction theory”. In: *The Philosophical Magazine: A Journal of Theoretical, Experimental and Applied Physics* 18.151 (1968), pp. 115–122. DOI: [10.1080/14786436808227313](https://doi.org/10.1080/14786436808227313).

[13] Gustav Albrecht. “The Absorption Factor in Crystal Spectroscopy”. In: *Review of Scientific Instruments* 10.8 (1939), pp. 221–222. DOI: [10.1063/1.1751537](https://doi.org/10.1063/1.1751537).

[14] E. van Genderen et al. “Ab initio structure determination of nanocrystals of organic pharmaceutical compounds by electron diffraction at room temperature using a Timepix quantum area direct electron detector”. In: *Acta Crystallographica Section A: Foundations and Advances* 72.2 (2016), pp. 236–242. DOI: [10.1107/S2053273315022500](https://doi.org/10.1107/S2053273315022500).

[15] Petra Simoncic et al. “Electron crystallography and dedicated electron-diffraction instrumentation”. In: *Acta Crystallographica Section E: Crystallographic Communications* 79 (2023), pp. 410–422. DOI: [10.1107/S2056989023003109](https://doi.org/10.1107/S2056989023003109).

[16] Helen W. Leung et al. “From formulation to structure: 3D electron diffraction for the structure solution of a new indomethacin polymorph from an amorphous solid dispersion”. In: *IUCrJ* 11 (2024), pp. 744–748. DOI: [10.1107/S2052252524005487](https://doi.org/10.1107/S2052252524005487).

[17] D. M. Bird and M. Saunders. “Sensitivity and accuracy of CBED pattern matching”. In: *Ultramicroscopy* 45.2 (Sept. 1992), pp. 241–251. DOI: [10.1016/0304-3991\(92\)90512-I](https://doi.org/10.1016/0304-3991(92)90512-I).

[18] J. M. Zuo and J. C. H. Spence. “Automated structure factor refinement from convergent-beam patterns”. In: *Ultramicroscopy* 35.3–4 (June 1991), pp. 185–196. DOI: [10.1016/0304-3991\(91\)90071-D](https://doi.org/10.1016/0304-3991(91)90071-D).

[19] P. A. Midgley et al. “Energy-filtered convergent-beam diffraction: examples and future prospects”. In: *Ultramicroscopy* 59.1–4 (July 1995), pp. 1–13. DOI: [10.1016/0304-3991\(95\)00014-R](https://doi.org/10.1016/0304-3991(95)00014-R).

[20] J. M. Zuo et al. “Direct observation of d-orbital holes and Cu–Cu bonding in Cu<sub>2</sub>O”. In: *Nature* 401 (Sept. 1999), pp. 49–52. DOI: [10.1038/43403](https://doi.org/10.1038/43403).

[21] Philip N. H. Nakashima et al. “A refinable three-parameter equation for phenomenological absorption in quantitative electron microscopy – determining the equation”. In: *Journal of Applied Crystallography* 58.5 (Oct. 2025), pp. 1665–1676. DOI: [10.1107/S160057672500545X](https://doi.org/10.1107/S160057672500545X).

[22] Moses Blackman. “On the intensities of electron diffraction rings”. In: *Proceedings of the Royal Society A* 173.952 (Nov. 1939), pp. 68–82. DOI: [10.1098/rspa.1939.0129](https://doi.org/10.1098/rspa.1939.0129).

[23] H. Hashimoto et al. “Anomalous electron absorption effects in metal foils: theory and comparison with experiment”. In: *Proceedings of the Royal Society of London. Series A. Mathematical and Physical Sciences* 269.1336 (Aug. 1962), pp. 67–87. DOI: 10.1098/rspa.1962.0164.

[24] Z. L. Wang. “Dynamical Simulations of Energy-Filtered Inelastic Electron Diffraction Patterns”. In: *Acta Crystallographica Section A* 48 (1992), pp. 674–688. DOI: 10.1107/S0108767392005791.

[25] Alexander S. Eggeman et al. “Measurement of molecular motion in organic semiconductors by thermal diffuse electron scattering”. In: *Nature Materials* 12 (July 2013), pp. 1045–1049. DOI: 10.1038/nmat3690.

[26] H. Bethe. “Zur Theorie des Durchgangs schneller Korpuskularstrahlen durch Materie”. In: *Annalen der Physik* 392 (1928), pp. 55–129. DOI: 10.1002/andp.19283920202.

[27] Hide Yoshioka. “Effect of Inelastic Waves on Electron Diffraction”. In: *Journal of the Physical Society of Japan* 12.6 (June 1957), pp. 618–628. DOI: 10.1143/JPSJ.12.618.

[28] D. M. Bird and Q. A. King. “Absorptive Form Factors for High-Energy Electron Diffraction”. In: *Acta Crystallographica Section A: Foundations of Crystallography* 46 (1990), pp. 202–208. DOI: 10.1107/S0108767390000502.

[29] Lian-Mao Peng. “Anisotropic Thermal Vibrations and Dynamical Electron Diffraction by Crystals”. In: *Acta Crystallographica Section A: Foundations of Crystallography* 53 (1997), pp. 663–672. DOI: 10.1107/S0108767397004907.

[30] Zhong Lin Wang. *Elastic and Inelastic Scattering in Electron Diffraction and Imaging*. English. Includes bibliographical references and index. New York; London: Plenum Press, 1995.

[31] L. J. Allen et al. “Modelling the inelastic scattering of fast electrons”. In: *Ultramicroscopy* 151 (Apr. 2015), pp. 11–22. DOI: 10.1016/j.ultramic.2014.10.011.

[32] Takashi Yamazaki et al. “Bloch wave simulations in the frozen lattice approximation”. In: *Ultramicroscopy* 135 (2013), pp. 16–23. DOI: <https://doi.org/10.1016/j.ultramic.2013.05.018>.

[33] Budhika G. Mendis. “A physical optics formulation of Bloch waves and its application to 4D STEM, 3D ED and inelastic scattering simulations”. In: *Acta Crystallographica Section A* 81.2 (Mar. 2025), pp. 113–123. DOI: 10.1107/S2053273325000142.

- [34] D. Rez et al. “Dirac–Fock calculations of X-ray scattering factors and contributions to the mean inner potential for electron scattering”. In: *Acta Crystallographica Section A* 50.4 (1994), pp. 481–497. DOI: <https://doi.org/10.1107/S0108767393013200>. eprint: <https://onlinelibrary.wiley.com/doi/pdf/10.1107/S0108767393013200>.
- [35] P. B. Hirsch et al. *Electron Microscopy of Thin Crystals*. London: Butterworths, 1965, p. 549.
- [36] G. J. McIntyre and R. F. D. Stansfield. “A general Lorentz correction for single-crystal diffractometers”. In: *Acta Crystallographica Section A* 44.3 (May 1988), pp. 257–262. DOI: [10.1107/S0108767387011656](https://doi.org/10.1107/S0108767387011656).
- [37] Daliang Zhang et al. In: *Zeitschrift für Kristallographie* 225.2-3 (2010), pp. 94–102. DOI: [doi:10.1524/zkri.2010.1202](https://doi.org/10.1524/zkri.2010.1202).
- [38] Alexander T. Holmes. “Simple Bayesian method for improved analysis of quasi-two-dimensional scattering data”. In: *Phys. Rev. B* 90 (2 July 2014), p. 024514. DOI: [10.1103/PhysRevB.90.024514](https://doi.org/10.1103/PhysRevB.90.024514).
- [39] Paul B. Klar et al. “Accurate structure models and absolute configuration determination using dynamical effects in continuous-rotation 3D electron diffraction data”. In: *Nature Chemistry* 15.6 (June 2023). Number: 6 Publisher: Nature Publishing Group, pp. 848–855. DOI: [10.1038/s41557-023-01186-1](https://doi.org/10.1038/s41557-023-01186-1).
- [40] Lukáš Palatinus et al. “Specifics of the data processing of precession electron diffraction tomography data and their implementation in the program PETS2.0”. In: *Acta Crystallographica Section A: Structural Science, Crystal Engineering and Materials* 75.4 (Aug. 2019), pp. 512–522. DOI: [10.1107/S2052520619007775](https://doi.org/10.1107/S2052520619007775).
- [41] Petr Brázda et al. “Electron diffraction determines molecular absolute configuration in a pharmaceutical nanocrystal”. In: *Science* 364 (2019), pp. 667–669. DOI: [10.1126/science.aaw2560](https://doi.org/10.1126/science.aaw2560).

# Supplementary Information: The role of absorption in dynamical three-dimensional electron-diffraction structure refinement

Benjamin Colmey<sup>1</sup>, Tiarnan A.S. Doherty<sup>1,2</sup>, Shreshth A. Malik<sup>2</sup>, and Paul A. Midgley<sup>1</sup>

<sup>1</sup>Department of Materials Science and Metallurgy, University of Cambridge, 27 Charles Babbage Rd, Cambridge, CB3 0FS, United Kingdom

<sup>2</sup>OATML, Department of Computer Science, University of Oxford, Wolfson Building, Parks Rd, Oxford, OX1 3QG, United Kingdom

## Overview

This Supplementary Information provides additional figures, derivations, simulation parameters and results supporting the main manuscript.

## 1 Derivation of the Two-Beam Integrated Intensity in the Presence of Absorption

Beginning from the modified two-beam expression for the diffracted-beam intensity under absorption:

$$|\psi_g|_{\text{abs}}^2 = e^{-2\kappa_0 t} \frac{1}{2} \left[ \frac{\cosh(2\Delta\kappa t)}{1+x^2} - \frac{\cos(2\pi\Delta k t)}{1+x^2} \right]. \quad (\text{S1})$$

Using the identities

$$\cosh 2\theta = 1 + 2 \sinh^2 \theta, \quad \cos 2\theta = 1 - 2 \sin^2 \theta,$$

we obtain

$$|\psi_g|_{\text{abs}}^2 = e^{-2\kappa_0 t} \left[ \frac{\sinh^2(\Delta\kappa t)}{1+x^2} + \frac{\sin^2(\pi\Delta k t)}{1+x^2} \right]. \quad (\text{S2})$$

where

$$\Delta\kappa = \frac{\pi}{\xi'_g \sqrt{1+x^2}}, \quad \Delta k = \frac{\sqrt{1+x^2}}{\xi_g}, \quad x = S_g \xi_g.$$

$$\frac{\sinh^2(\Delta\kappa t)}{1+x^2} = \frac{\sinh^2(B(1+x^2)^{-1/2})}{1+x^2}, \quad B = \frac{\pi t}{\xi'_g}. \quad (\text{S3})$$

$$\frac{\sin^2(\pi\Delta k t)}{1+x^2} = \frac{\sin^2(A(1+x^2)^{1/2})}{1+x^2}, \quad A = \frac{\pi t}{\xi_g}. \quad (\text{S4})$$

Thus the absorbed integrated intensity is

$$I_{\text{abs}}^{\text{int}}(t) = \int_{-\infty}^{\infty} |\psi_g|_{\text{abs}}^2 dx = e^{-2\kappa_0 t} \{(1) + (2)\}, \quad dx = \xi_g dS_g. \quad (\text{S5})$$

$$(1) = \int_{-\infty}^{\infty} \frac{\sin^2(A(1+x^2)^{1/2})}{1+x^2} dx = 2 \int_0^A J_0(2x) dx. \quad (\text{S6})$$

For  $A = \pi t/\xi_g \ll 1$ ,

$$J_0(2x) = 1 - x^2/4 + \dots,$$

$$(1) = A - \frac{A^3}{12} = \frac{\pi t}{\xi_g} \left( 1 - \frac{\pi^2 t^2}{12 \xi_g^2} \right). \quad (\text{S7})$$

$$(2) = \int_{-\infty}^{\infty} \frac{\sinh^2(B(1+x^2)^{-1/2})}{1+x^2} dx. \quad (\text{S8})$$

Since  $B = \pi t/\xi'_g \ll 1$ ,

$$\sinh^2 \theta \approx \theta^2 \quad (\text{keeping only first order term}), \quad \theta = B(1+x^2)^{-1/2},$$

$$(2) \approx \int_{-\infty}^{\infty} \frac{B^2}{(1+x^2)^2} dx = B^2 \frac{\pi}{2} = \frac{\pi^3 t^2}{2 \xi'_g}. \quad (\text{S9})$$

The non-absorbed integrated intensity is

$$I_{\text{no abs}}^{\text{int}}(t) = \int_{-\infty}^{\infty} |\psi_g|_{\text{no abs}}^2 dx = (1). \quad (\text{S10})$$

$$\frac{I_{\text{abs}}^{\text{int}}(t)}{I_{\text{no abs}}^{\text{int}}(t)} = \frac{e^{-2\kappa_0 t} \{(1) + (2)\}}{(1)} = e^{-2\kappa_0 t} \left[ 1 + \frac{(2)}{(1)} \right]. \quad (\text{S11})$$

$$\frac{(2)}{(1)} = \frac{\frac{\pi^3 t^2}{2 \xi'_g}}{\frac{\pi t}{\xi_g} \left( 1 - \frac{\pi^2 t^2}{12 \xi_g^2} \right)} = \frac{\pi^2 t \xi_g}{2 \xi'_g} \left( 1 - \frac{\pi^2 t^2}{12 \xi_g^2} \right)^{-1}. \quad (\text{S12})$$

$$\frac{I_{\text{abs}}^{\text{int}}(t)}{I_{\text{no abs}}^{\text{int}}(t)} = e^{-2\kappa_0 t} \left[ 1 + \frac{\pi^2 t \xi_g}{2\xi_g'^2} \left( 1 - \frac{\pi^2 t^2}{12\xi_g^2} \right)^{-1} \right] \quad (\text{S13})$$

To assess the validity of Eq. S13, its thickness dependence is examined alongside the ratio of intensities computed by numerical integration of Main Text Eqs. 4 and 6.

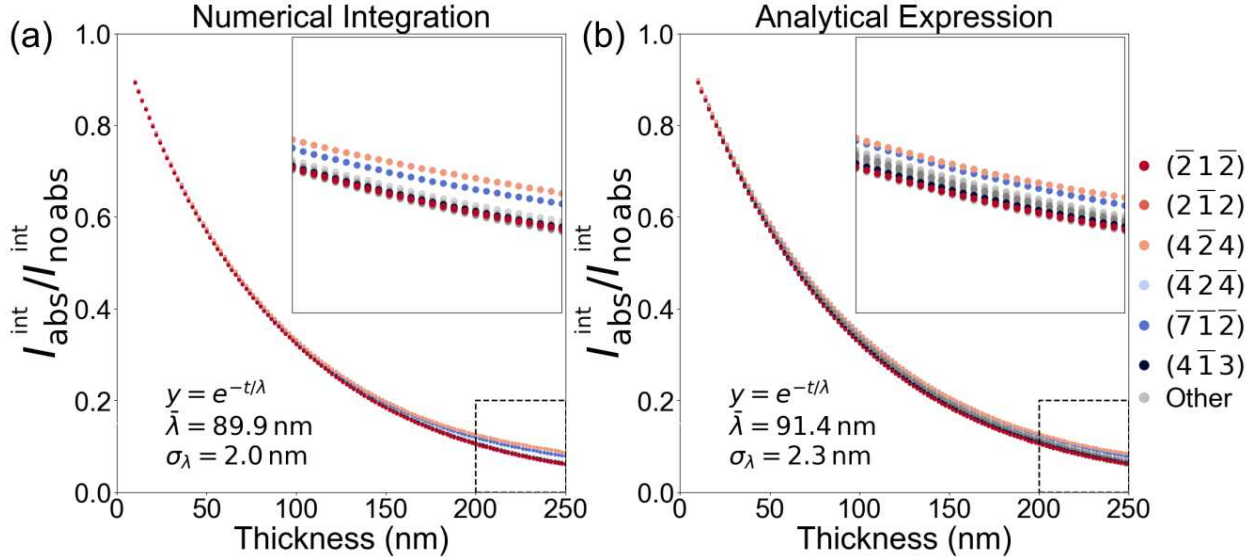


Figure S1: Comparison of  $I_{\text{abs}}^{\text{int}}/I_{\text{no abs}}^{\text{int}}$  for the two-beam model. (a) Numerical integration, with an inset showing the high-thickness region. (b) Analytic approximation given by Eq. S13.

## 2 Derivation of $R_1(t)$ in terms of $\bar{\lambda}$ and $\sigma_\lambda$

The  $R$ -factor is defined as

$$R_1(t) = \frac{\sum_i |\sqrt{I_i^{\text{abs}}(t)} - \sqrt{I_i^{\text{no abs}}}|}{\sum_i \sqrt{I_i^{\text{no abs}}}}, \quad (\text{S14})$$

where  $I_i^{\text{no abs}}$  is the intensity without absorption, and

$$I_i^{\text{abs}}(t) = I_i^{\text{no abs}} e^{-t/\lambda_i} \quad (\text{S15})$$

As the mean absorption length  $\bar{\lambda}$  scales all intensities equally, it does not contribute to the per-reflection variation and thus has no effect on  $R(t)$ . Its contribution can therefore be removed with a global scaling factor. The scaled absorbed intensity is

$$I_i^{\text{abs, scaled}}(t) = I_i^{\text{no abs}} \frac{e^{-t/\lambda_i}}{e^{-t/\bar{\lambda}}}, \quad (\text{S16})$$

so that

$$\sqrt{I_i^{\text{abs, scaled}}(t)} = \sqrt{I_i^{\text{no abs}}} e^{-\frac{t}{2}(X_i - \mu_X)}, \quad X_i = \frac{1}{\lambda_i}, \quad \mu_X = \frac{1}{\bar{\lambda}}. \quad (\text{S17})$$

Substituting into (S14) gives

$$R_1(t) = \sum_i w_i \left| e^{-\frac{t}{2}(X_i - \mu_X)} - 1 \right|, \quad w_i = \frac{\sqrt{I_i^{\text{no abs}}}}{\sum_j \sqrt{I_{0,j}}}. \quad (\text{S18})$$

For small  $t(X_i - \mu_X)$  the exponential can be expanded:

$$e^{-\frac{t}{2}(X_i - \mu_X)} \approx 1 - \frac{t}{2}(X_i - \mu_X), \quad (\text{S19})$$

so that

$$R_1(t) \approx \frac{t}{2} \sum_i w_i |X_i - \mu_X|. \quad (\text{S20})$$

The weighted variance is defined as

$$\sigma_X^2 = \sum_i w_i (X_i - \mu_X)^2, \quad (\text{S21})$$

and the standardized variables as

$$Z_i = \frac{X_i - \mu_X}{\sigma_X}, \quad \sum_i w_i Z_i^2 = 1, \quad (\text{S22})$$

which yield

$$\sum_i w_i |X_i - \mu_X| = \sigma_X \sum_i w_i |Z_i|. \quad (\text{S23})$$

If the distribution of  $X_i$  is approximately Gaussian, the standardized values behave like samples from  $Z \sim \mathcal{N}(0, 1)$ , for which the expectation can be found:

$$\mathbb{E}[|Z|] = \int_{-\infty}^{\infty} |z| \frac{1}{\sqrt{2\pi}} e^{-z^2/2} dz = \sqrt{\frac{2}{\pi}}. \quad (\text{S24})$$

Hence,

$$\sum_i w_i |X_i - \mu_X| \approx \sigma_X \sqrt{\frac{2}{\pi}}, \quad R_1(t) \approx \frac{t}{2} \sqrt{\frac{2}{\pi}} \sigma_X. \quad (\text{S25})$$

The quantity  $\sigma_X$  may now be related to  $\sigma_\lambda$  to express the result in terms of the absorption lengths. Writing  $\lambda = \bar{\lambda} + \delta\lambda$ , a first-order expansion gives

$$X = \frac{1}{\lambda} \approx \frac{1}{\bar{\lambda}} - \frac{\delta\lambda}{\bar{\lambda}^2}, \quad X - \mu_X \approx -\frac{\delta\lambda}{\bar{\lambda}^2}. \quad (\text{S26})$$

Squaring and averaging,

$$\sigma_X^2 = \mathbb{E}[(X - \mu_X)^2] \approx \frac{1}{\bar{\lambda}^4} \mathbb{E}[(\delta\lambda)^2]. \quad (\text{S27})$$

By definition,

$$\mathbb{E}[(\delta\lambda)^2] = \sigma_\lambda^2, \quad (\text{S28})$$

and therefore

$$\sigma_X \approx \frac{\sigma_\lambda}{\bar{\lambda}^2}. \quad (\text{S29})$$

Substituting (S29) into (S25) yields the final result:

$$R_1(t) \approx \sqrt{\frac{2}{\pi}} \frac{t \sigma_\lambda}{2 \bar{\lambda}^2}. \quad (\text{S30})$$

### 3 Supplementary Figures

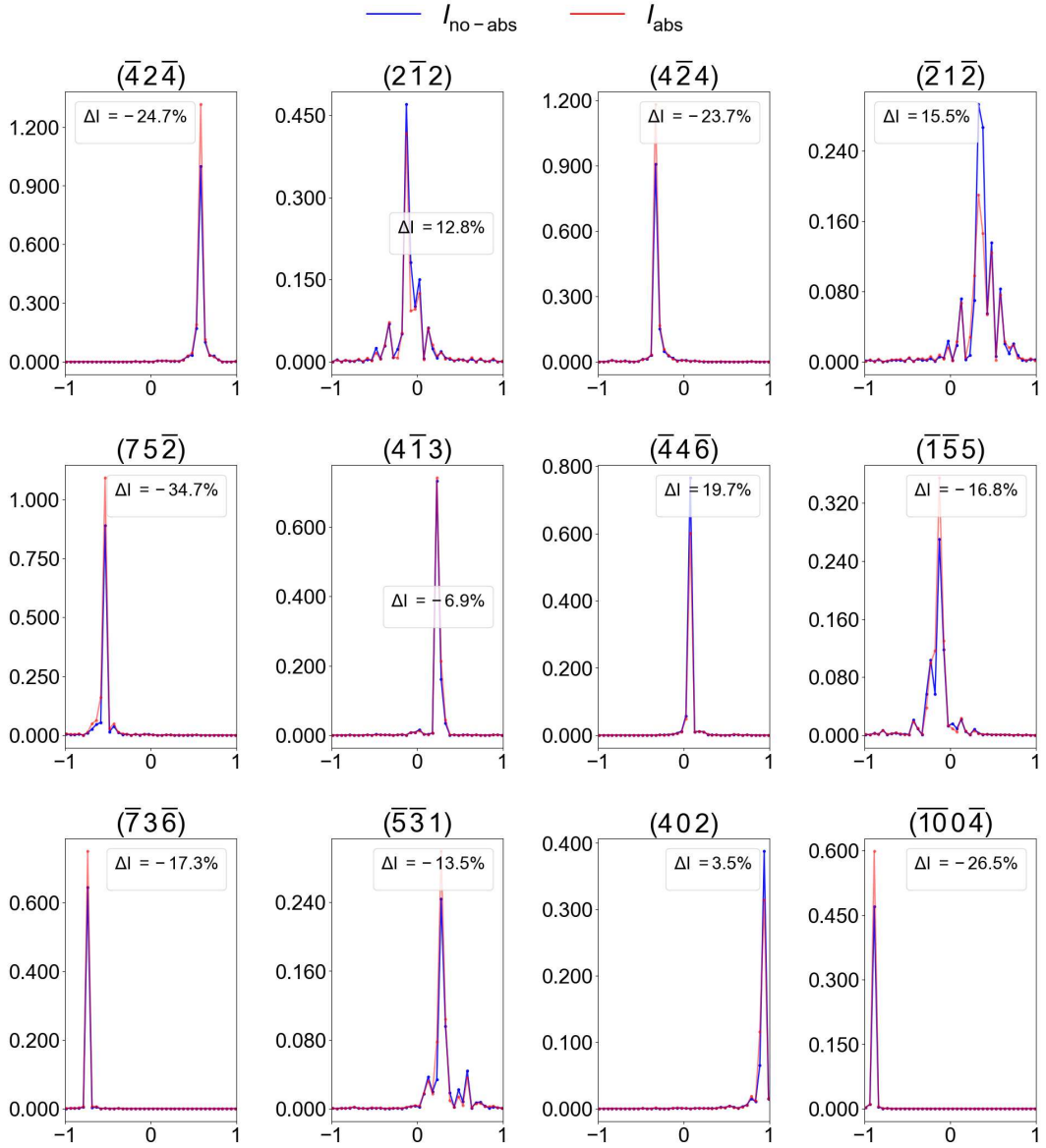


Figure S2: Many-beam rocking curves for  $\text{CsPbBr}_3$  at  $t = 200 \text{ nm}$ ,  $200 \text{ keV}$ , and  $[uvw] = [-0.43, 1.00, 0.93]$  (page 1 of 3). For clarity, the  $x$ -axis is limited to  $\pm 1^\circ$ , while the underlying simulation extends to  $\pm 1.5^\circ$ . The absorptive curves are scaled by a physical de-attenuation factor  $\exp(t/\lambda)$  with  $t = 200 \text{ nm}$  and  $\lambda = 88.4 \text{ nm}$  to compensate for uniform absorption due to  $U'_0$ ;  $\Delta I$  gives the % difference between integrated values after this correction:  $\Delta I = 100 \times \frac{I_{\text{no-abs}} - I_{\text{abs}}}{I_{\text{no-abs}}}$ .

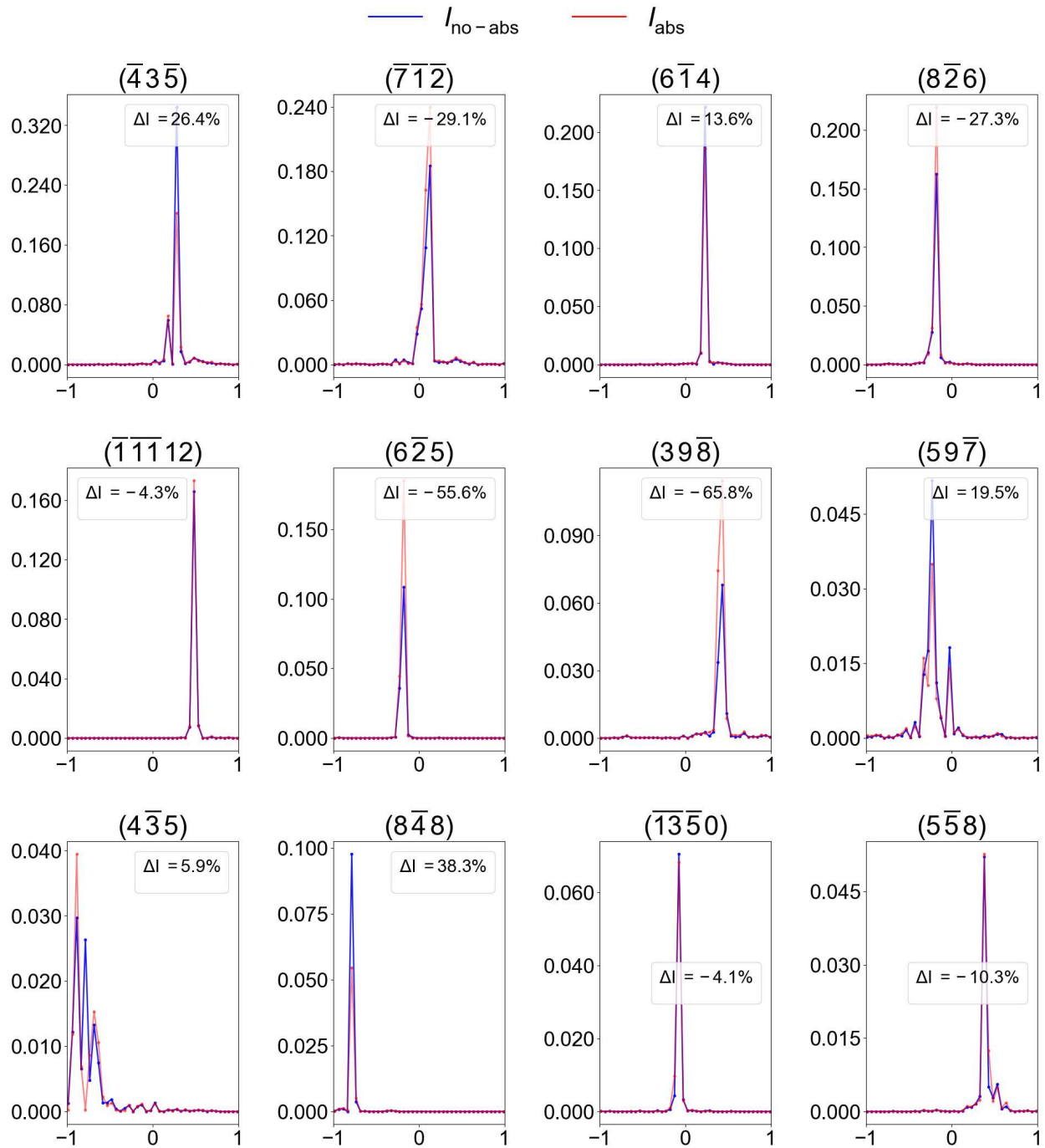


Figure S2: (continued, page 2 of 3).

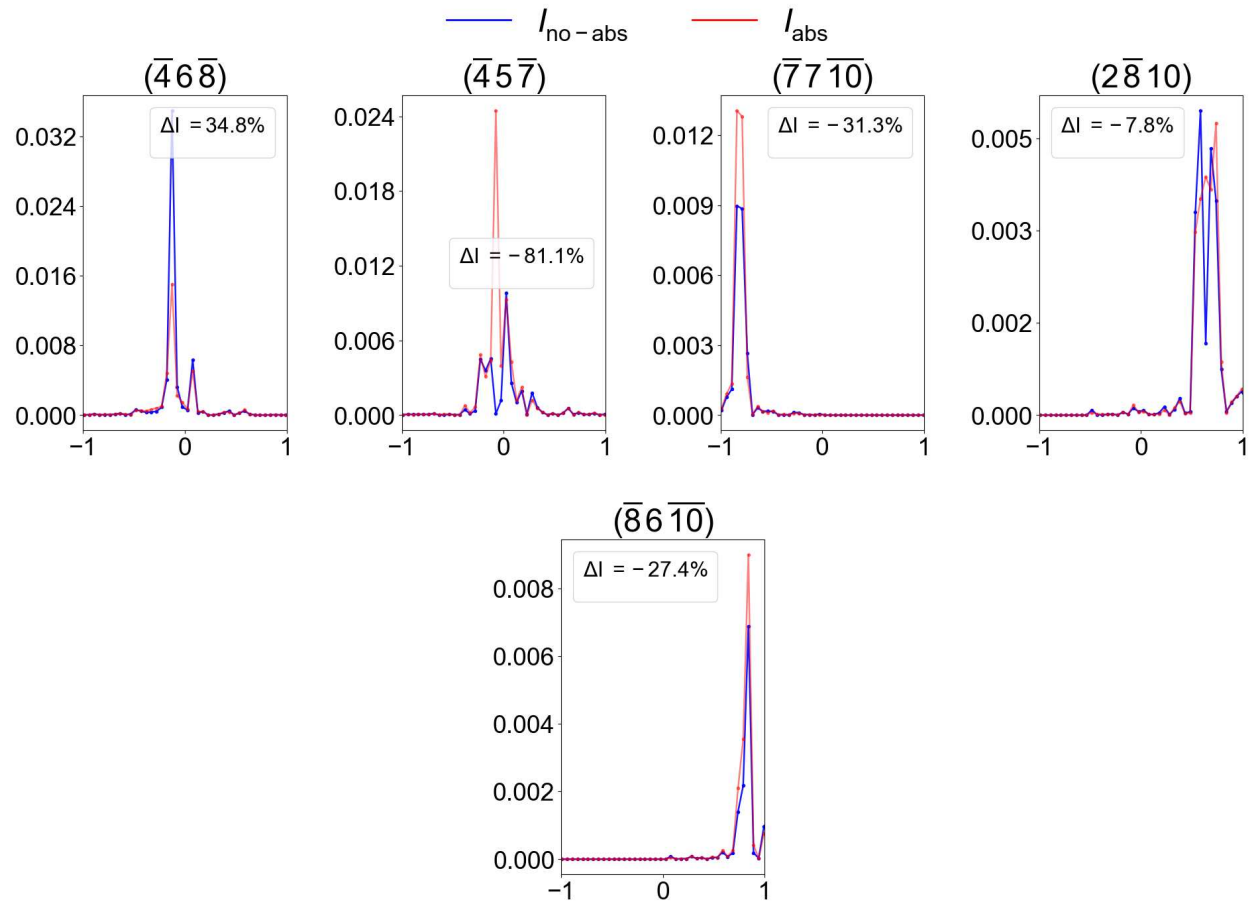


Figure S2: (continued, page 3 of 3).

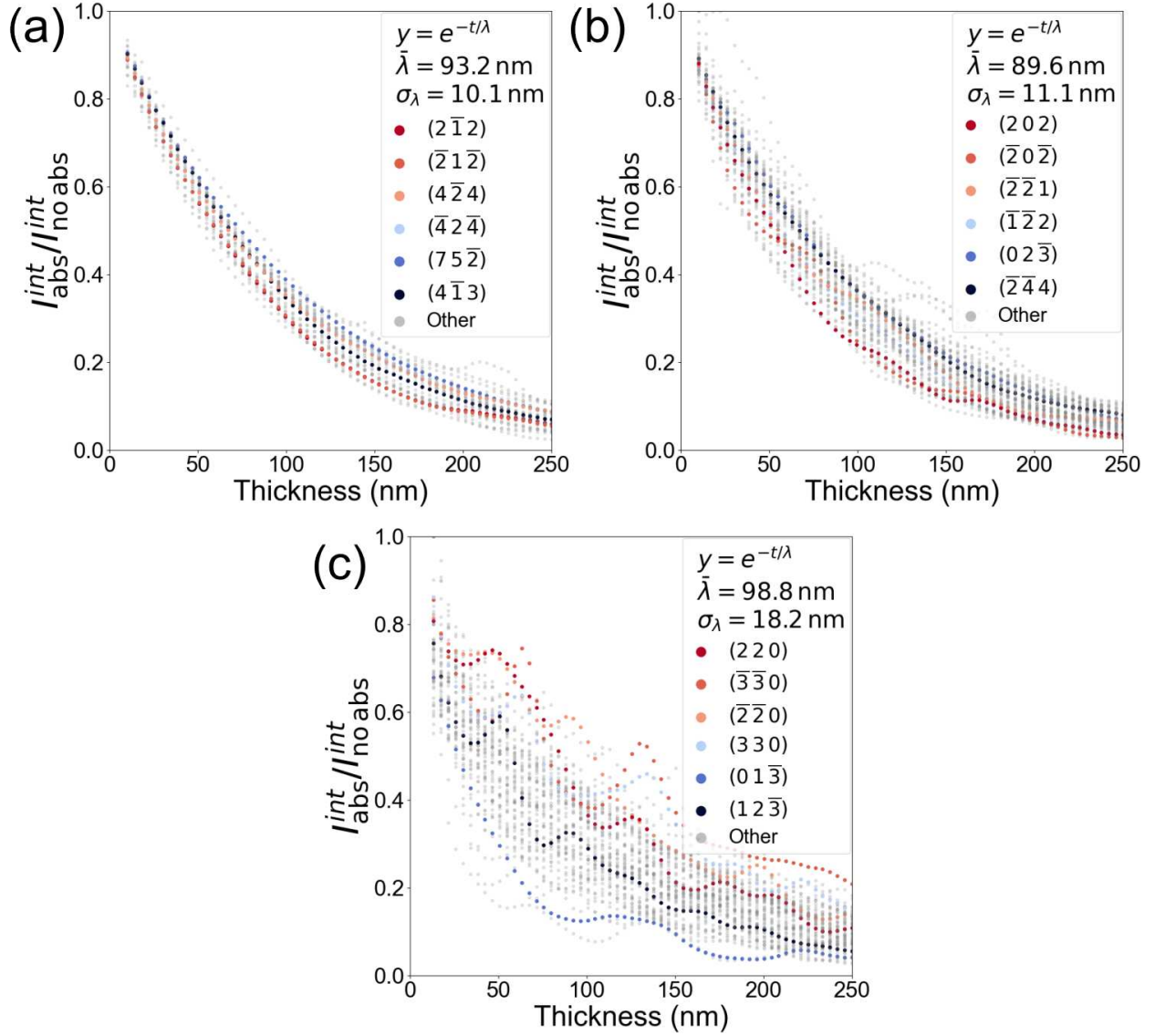


Figure S3: Orientation dependence of absorption effects in  $\text{CsPbBr}_3$ . (a–c) Ratio of integrated intensities  $I_{\text{abs}}/I_{\text{no abs}}$  as a function of thickness from many-beam dynamical diffraction simulations for orientations 1, 8, and 19. The six most intense reflections are highlighted in colour, with all others shown in grey. Mean absorption length  $\bar{\lambda}$  and standard deviation  $\sigma_{\lambda}$  are shown for each orientation.

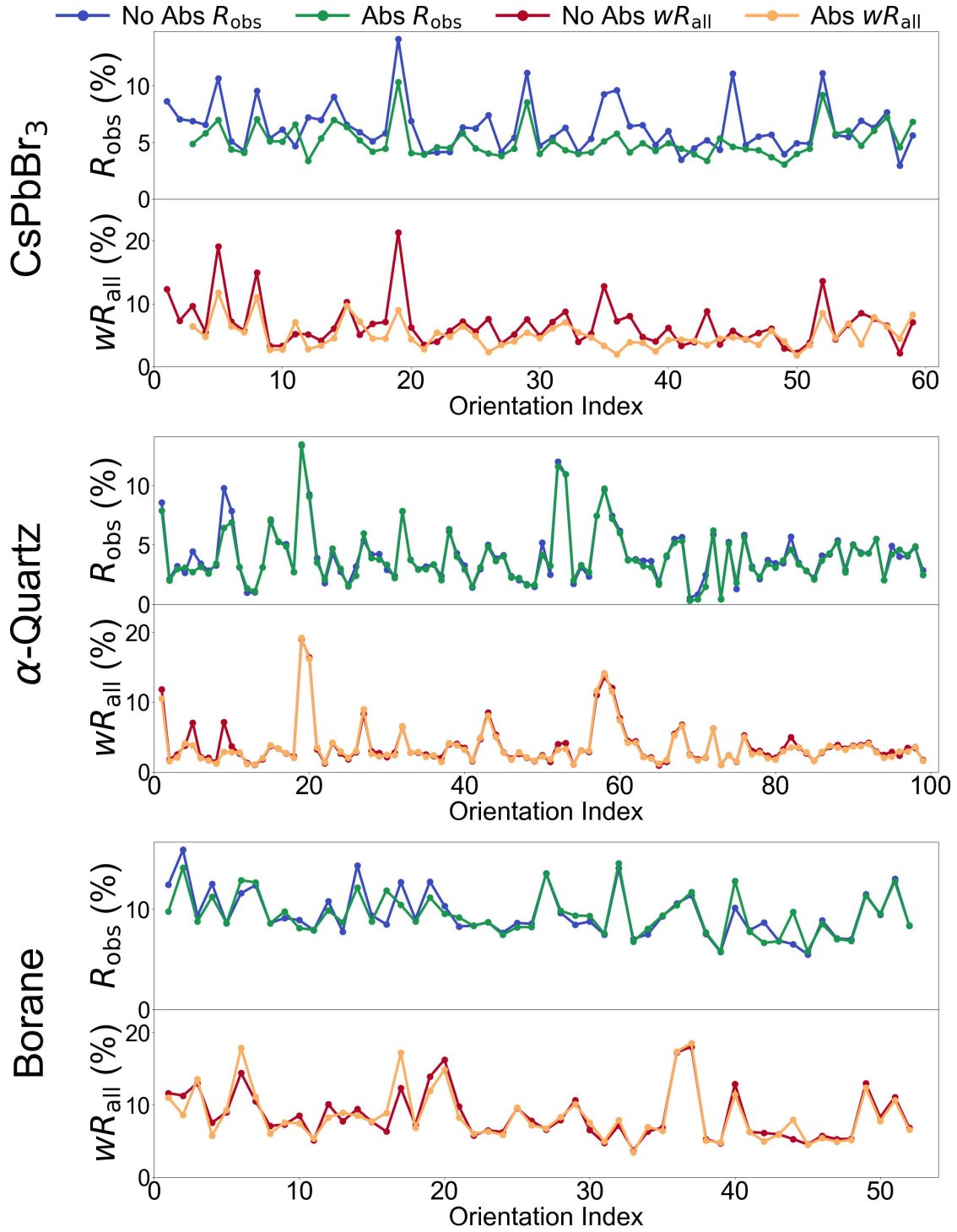


Figure S4: Results of dynamical refinements performed with and without absorption for  $\text{CsPbBr}_3$ ,  $\alpha$ -quartz, and borane. Residuals  $R_{\text{obs}}$  and  $wR_{\text{all}}$  are shown across all rotation indices for refinements carried out on identical datasets and parameters.

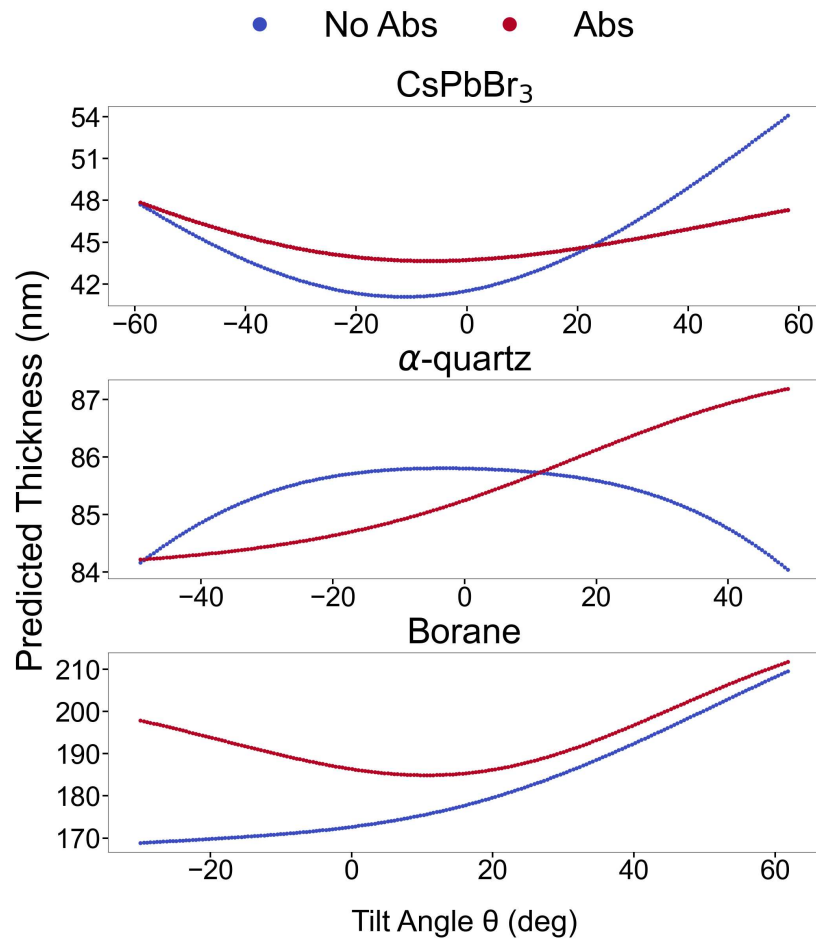


Figure S5: Experimental thickness curves recovered from dynamical refinements performed with and without absorption for CsPbBr<sub>3</sub>,  $\alpha$ -quartz, and borane datasets.

## 4 Supplementary Tables

Table S1: Summary of Main Text Fig. 3 (b): material dependence of absorption effects, showing slopes of  $R_1(t)$  (%/nm) for representative orientations. Mean atomic number  $\langle Z \rangle$ , reported thickness  $t_{\text{obs}}$ , and the predicted contribution of absorption to  $R_{\text{obs}}$  are also listed.

Material	$\langle Z \rangle$	$t_{\text{obs}}$ (nm)	Orientations [uvw]	$dR_1/dt$ (%/nm)	Pred. (%)
<b>CsPbBr<sub>3</sub></b>	48.4	48.0	[-0.43, 1.00, 0.93]	0.0480	2.11
			[-0.46, 1.00, 0.89]	0.0418	1.83
			[-0.50, 1.00, 0.85]	0.0405	1.78
<b><math>\alpha</math>-Quartz</b>	10.0	85.0	[-1.00, 0.08, -0.28]	0.0064	0.74
			[-1.00, 0.10, -0.29]	0.0058	0.65
			[-1.00, 0.13, -0.29]	0.0046	0.52
<b>Borane</b>	2.8	170.0	[1.00, -0.49, -0.52]	0.0004	0.12,
			[1.00, -0.46, -0.54]	0.0009	0.20
			[1.00, -0.43, -0.57]	0.007	0.17

Table S2: Refinement parameters and residuals for  $\text{CsPbBr}_3$ ,  $\alpha$ -quartz, and borane. All settings are identical between elastic-only and absorptive refinements. Geometric filtering parameters  $RS_g$  and  $DS_g$  follow the conventions of (Klar et al., 2023). Values denoted with (SFs) refer to the maximum resolution included in structure factor calculations.

Parameter	$\text{CsPbBr}_3$	$\alpha$ -quartz	Borane
Integration semiangle (°)	1.5	1.0	1.35
Rocking-curve sampling	60	42	125
$D_{sg}$	0.0015	0.0015	0.00
$R_{sg}$	0.66	0.90	0.66
$g_{\max}$ (SFs) $\text{\AA}^{-1}$	2.5	2.5	2.5
$g_{\max}^{\text{refine}}$ $\text{\AA}^{-1}$	2.0	1.6	1.7
$S_g^{\max}$ (SFs) $\text{\AA}^{-1}$	0.2	0.1	0.1
<b>Elastic-only refinement</b>			
$R_{\text{obs}}$ (%)	6.40	4.12	9.54
$wR_{\text{all}}$ (%)	6.73	3.84	8.56
<b>Absorptive refinement</b>			
$R_{\text{obs}}$ (%)	5.26	4.00	9.48
$wR_{\text{all}}$ (%)	5.31	3.66	8.51

Table S3: Fractional atomic coordinates and anisotropic displacement parameters from dynamical refinements of  $\text{CsPbBr}_3$  performed with and without inclusion of absorption.

Atom	Without Absorption						With Absorption					
	$x$	$y$	$z$	$U_{11}$	$U_{22}$	$U_{33}$	$x$	$y$	$z$	$U_{11}$	$U_{22}$	$U_{33}$
Cs	0.514	0.553	0.750	0.045	0.039	0.028	0.514	0.554	0.750	0.044	0.042	0.030
Pb	0.500	0.000	0.500	0.016	0.014	0.014	0.500	0.000	0.500	0.016	0.014	0.014
Br1	0.301	0.701	0.468	0.023	0.023	0.035	0.301	0.701	0.468	0.024	0.022	0.036
Br2	0.439	0.995	0.750	0.043	0.044	0.012	0.440	0.995	0.750	0.046	0.046	0.011

Table S4: Fractional atomic coordinates and anisotropic displacement parameters from dynamical refinements of quartz with and without absorption.

Atom	Without Absorption						With Absorption					
	<i>x</i>	<i>y</i>	<i>z</i>	<i>U</i> <sub>11</sub>	<i>U</i> <sub>22</sub>	<i>U</i> <sub>33</sub>	<i>x</i>	<i>y</i>	<i>z</i>	<i>U</i> <sub>11</sub>	<i>U</i> <sub>22</sub>	<i>U</i> <sub>33</sub>
Si	0.7644	0.4081	0.8333	0.0105	0.0109	0.0049	0.7644	0.4081	0.8333	0.0108	0.0112	0.0052
O	0.5621	0.5072	0.6189	0.0105	0.0194	0.0161	0.5619	0.5074	0.6189	0.0113	0.0197	0.0160

Table S5: Fractional atomic coordinates and anisotropic displacement parameters from dynamical refinements of borane with and without absorption.

Atom	Without Absorption						With Absorption					
	<i>x</i>	<i>y</i>	<i>z</i>	<i>U</i> <sub>11</sub>	<i>U</i> <sub>22</sub>	<i>U</i> <sub>33</sub>	<i>x</i>	<i>y</i>	<i>z</i>	<i>U</i> <sub>11</sub>	<i>U</i> <sub>22</sub>	<i>U</i> <sub>33</sub>
H1	0.4255	0.4902	0.2342	0.0226	0.0140	0.0596	0.4256	0.4901	0.2341	0.0230	0.0150	0.0611
H2	0.5413	0.5880	0.1026	0.1359	0.0533	0.0036	0.5411	0.5881	0.1026	0.1460	0.0660	0.0098
H3	0.7160	0.6490	0.3212	0.0481	0.0250	0.0738	0.7158	0.6493	0.3211	0.0475	0.0325	0.0782
H4	0.6173	0.2361	0.3329	0.0767	0.0176	0.0479	0.6166	0.2366	0.3331	0.0676	0.0175	0.0505
H5	0.7863	0.4412	0.4552	0.0469	0.0675	0.0335	0.7856	0.4410	0.4551	0.0496	0.0824	0.0261
H6	0.5307	0.6140	0.2931	0.0185	0.0197	0.0062	0.5314	0.6137	0.2935	0.0214	0.0166	0.0072
H7	0.4569	0.3396	0.1401	0.0437	0.0477	0.0153	0.4571	0.3400	0.1405	0.0331	0.0539	0.0124
H8	0.7439	0.4082	0.1791	0.0593	0.0791	0.0333	0.7440	0.4083	0.1789	0.0559	0.0713	0.0322
H9	0.3542	0.4459	0.3981	0.0310	0.0063	0.0960	0.3542	0.4462	0.3987	0.0331	0.0105	0.0983
H10	0.5886	0.3199	0.5888	0.0551	0.0703	0.1194	0.5884	0.3201	0.5884	0.0434	0.0709	0.1046
H11	0.3605	0.2708	0.4084	0.0298	0.0393	0.1378	0.3608	0.2705	0.4082	0.0386	0.0354	0.1238
B1	0.4328	0.3541	0.3945	0.0012	0.0047	0.0147	0.4327	0.3541	0.3946	0.0015	0.0063	0.0147
B2	0.6797	0.4485	0.4129	0.0034	0.0083	0.0051	0.6796	0.4481	0.4130	0.0033	0.0082	0.0053
B3	0.5446	0.5353	0.2009	0.0072	0.0084	0.0147	0.5447	0.5352	0.2008	0.0049	0.0093	0.0158
B4	0.5891	0.3358	0.3469	0.0033	0.0005	0.0166	0.5890	0.3358	0.3472	0.0034	0.0009	0.0152
B5	0.6543	0.4398	0.2460	0.0078	0.0081	0.0075	0.6541	0.4396	0.2460	0.0072	0.0083	0.0089
B6	0.5582	0.3828	0.5000	0.0039	0.0054	0.0030	0.5581	0.3825	0.4999	0.0041	0.0049	0.0026
B7	0.6432	0.5702	0.3274	0.0016	0.0002	0.0199	0.6430	0.5702	0.3275	0.0014	0.0009	0.0203
B8	0.4953	0.3932	0.2292	0.0112	0.0082	0.0029	0.4955	0.3933	0.2293	0.0081	0.0064	0.0079
B9	0.5755	0.5322	0.4937	0.0005	0.0004	0.0127	0.5756	0.5325	0.4941	0.0005	0.0003	0.0132